Characterizing the onset of transitional and turbulent flow regimes in pipe flows using instantaneous time-frequency-based analysis

Nikhil Shirdade, Jibin Joy Kolliyil, Baha Al-Deen T. El-Khader, and Melissa C. Brindise*
Department of Mechanical Engineering,
The Pennsylvania State University,
University Park, PA 16802, USA

Accurately identifying the onset of transitional and turbulent flow within any pipe flow environment is of great interest. Most often, the critical Reynolds number (Re) is used to pinpoint the onset of turbulence. However, the critical Re is known to be highly variable, depending on the specifics of the flow system. Thus, for flows (e.g., blood flows), where only one realization (i.e., one mean Re) exists, the presence of transitional and turbulent flow behaviors cannot be accurately determined. In this work, we aim to address this by evaluating the extent to which instantaneous time-frequency (TF)-based analysis of the fluctuating velocity field can be used to evaluate the onset of transitional and turbulent flow regimes. Because current TF analysis methods are not suitable for this, we propose a novel 'wavelet-Hilbert time-frequency' (WHTF) method which we validate herein. Using the WHTF method, we analyzed the instantaneous dominant frequency of three planar particle image velocimetry-captured pipe flows which included one steady and two pulsatile with Womersley numbers of 4 and 12. For each case, data was captured at Re's spanning 800–4500. The instantaneous dominant frequency analysis of these flows revealed that the magnitude, size, and coherence of two-dimensional spatial frequency structures were uniquely different across flow regimes. Specifically, the transitional regime maintained the most coherent, but lowest magnitude frequency structures, while the laminar regime had the highest magnitude, lowest coherence, and smallest frequency structures. Overall, this study demonstrates the efficacy of TF-based metrics for characterizing the progression of transition and turbulent flow development.

I. INTRODUCTION

Transition to turbulence in pipe flows is characterized by intermittency [1–6]. At the onset of transitional flow, intermittent flow structures, or turbulent "puffs", begin to form at locations of instabilities. As transition develops, the puffs occur with increasing frequency until they form at such a high rate the individual puffs are no longer discernible, at which point the flow is classified as fully turbulent [7]. Transitional flow induces significant fluctuations in pressure and wall shear stress which negatively affect pipe wall strength, flow energy losses, etc. Thus, accurately identifying the onset of this flow regime is of great interest.

Traditionally, the onset of transitional and fully turbulent flow is estimated using the non-dimensional Reynolds number, $Re(=\rho UD/\mu)$, where, U is the mean velocity (m/s) of the flow, ρ (kg/m^3) is the density, D (m) is the diameter of the pipe, and μ $(Pa-s)$ is the dynamic viscosity of the fluid [8]. Many prior studies utilizing steady-mean and unsteady-mean (i.e. oscillating or pulsatile) pipe flows have ascertained the onset of transition to occur at a Re of about 2200–2500 and the critical Re, $Re_{critical}$, when flow becomes fully turbulent to be 2700–3000 [9, 10]. These values are generally determined by evaluating the turbulence intensity (TI) of a flow across a range of Re values. This TI–Re relationship is represented by an S-shaped curve where TI in the laminar and turbulent regimes is roughly independent of Re.

$Re_{critical}$ values are highly specific to specific flow environments; factors including pipe roughness, pump-induced perturbations, geometry irregularities, pipe curvature, etc. are all known to alter the $Re_{critical}$. Hence, it is widely accepted that significant variability from the consensus $Re_{critical}$ values can occur. The variability of $Re_{critical}$ leads to a significant fundamental challenge of how to determine if a specific flow is transitional in nature [11]. This is particularly consequential in cases where only one representation of the flow (i.e., the flow at one mean Re) is known. For example, in the biomedical domain, studies are increasingly asserting low Re flows to be transitional or fully turbulent. In one such study, Saqr *et al.* [12] evaluated the physiologic blood flow and concluded that an aneurysmal flow—which has significant cross-sectional variability—with a mean Re of about 300 was turbulent. Hence, this highlights an increasingly pressing need for universal metrics or characteristics capable of estimating the level of transitional flow behavior within any pipe flow environment.

Unfortunately, such a universal metric in pipe flows does not exist and methods to analyze transitional flows remain limited. Reported techniques to study transition to turbulence have involved the use of linearized Orr-Sommerfeld

* Corresponding Author: mcb5351@psu.edu

eigenvalue stability equations or viewing the flow as a dynamical system and finding the onset of chaos using bifurcation models [1]. However, these techniques are cumbersome and provide no visual information such that they cannot be employed to universally pinpoint the onset of transition and eventual culmination of a 2D flow to a 3D turbulence. Other studies have investigated the flow system as an excitable and bistable media because the localized puffs are generated and split throughout transition [2]. The increasing time fraction in which these puffs appear radially in the flow can also provide details regarding the onset of transition. This has been studied using Markov models as probability distribution functions [3]. Overall, these approaches make use of a particular variable and hence do not put forth a general trend in identifying a metric for the progression of transition.

Intermittency, by definition, suggests that transitional flow maintains characteristic frequencies [5, 13–15]. Thus, time-frequency (TF) methods can provide quantitative insight on the development and progression of transitional flow [16–21]. We previously demonstrated that TF analysis can be used to decompose the Kolmogorov spectrum in transitional flow, and by using this technique flow structures across energy scales could be isolated and visualized. Moreover, we showed that one instantaneous frequency (IF) appeared to primarily characterize the turbulent behavior within a pulsatile transitional flow in Joy Kolliyil *et al.* [22],[23]. These findings suggest the possibility that TF analysis can estimate the onset and progression of transition in a flow field. However, traditional TF approaches do not maintain the required visual information in conjunction with flow parameters such as velocity and fail to portray a complete analysis which puts forth a one-to-one mapping of frequency and flow parameters [24–26]. Some of the other investigations which have studied time-dependent flows and turbulent mixing in the literature include instability analysis such as Rayleigh-Taylor and Richtmyer–Meshkov instability.[27–29]

In this work, we aim to investigate the extent to which TF-based metrics can describe and identify the onset and level of development of transitional and turbulent pipe flows.

Two experimental datasets were used for this study. First, we conducted a steady-mean, planar particle image velocimetry (PIV) study with test cases spanning the Re_s range of 500 to 4500 such that the traditional TI vs Re S-curve could be established. Second, we utilized a pulsatile, transitional pipe flow dataset published in El-Khader and Brindise [30]. The pulsatile dataset was captured using planar PIV and the same experimental setup as used for the steady flow dataset. For both datasets, the instantaneous dominant frequency of the fluctuating velocity (u') field at each spatial point was evaluated using a novel time-frequency analysis method we propose and validate herein. We investigated how the TF representation of a flow differed in the laminar, transitional, and turbulent regimes. Specifically, we assessed the extent to which TF-based metrics reflected the traditional TI vs. Re S-curve and the extent to which the TF-metric values were "universal" across the different datasets used for testing herein.

Overall, this work takes a first step towards addressing the critical need for a universal metric to identify the onset and development of transitional and turbulent flow in pipe flows which can later be extended to any arbitrary flow environment.

II. PROPOSED INSTANTANEOUS TIME-FREQUENCY EVALUATION METHOD

For this work, we developed a novel time-frequency analysis method, which utilizes the continuous wavelet transform (CWT) [31–35] and Hilbert transform. We term this the Wavelet-Hilbert Time-Frequency (WHTF) method. The WHTF method, schematically shown in Fig. 1, is a computationally-light algorithm that computes the instantaneous dominant frequency at each point in space and time. The use of a computationally-light method herein ensures our findings are adaptable to complex flow environments of any Reynolds number and large datasets. The WHTF method iterates through each spatial point individually (Fig. 1(a)). The 1-D fluctuating velocity (u') vs time trend at the particular spatial point is the input to the calculation. The Hilbert transform of the fluctuating velocity signal is computed (Fig. 1(b)) and the CWT of this signal is evaluated (Fig. 1(c)). For the CWT computation, the Morlet wavelet was chosen as the mother wavelet due to its various advantages such as analyzing temporal behavior of non-stationary signals [36] and its shape function being similar to input pulsatile waveforms [37]. Additionally, using analytical signals with ground-truth frequencies, we tested the efficacy of other mother wavelets (e.g., 'Mexican Hat', 'Symlet') and found the Morlet to provide optimal performance accuracy and robustness. The scales of the CWT are uniformly defined from 0 to the Nyquist frequency for the given signal. The Hilbert Transform computes the analytical signal, resulting in both real and imaginary components with a 90^o phase shift. Hence, the CWT of the Hilbert transform of a signal results in a smooth coefficient field. The CWT of the raw signal would yield an intermittent dotted coefficient pattern even for constant frequency signals; this dotted pattern would be unsuitable for extracting the instantaneous dominant frequency. The combination of the Hilbert transform and CWT is computationally similar to a dual-tree wavelet transform. The evaluated CWT coefficient field is filtered using the discrete wavelet transform (DWT). Specifically, the 'sym8' wavelet is employed to smoothen the coefficients as the raw CWT coefficients can maintain noisy, high amplitude peaks in the frequency array. The 'sym8' was chosen as it has been shown to be optimal for signal denoising [38–40]. No forced denoising was employed in the filtering process. The filtered wavelet coefficient map is shown in Fig. 1(c) (Bottom). To evaluate the instantaneous dominant frequency, the largest peak

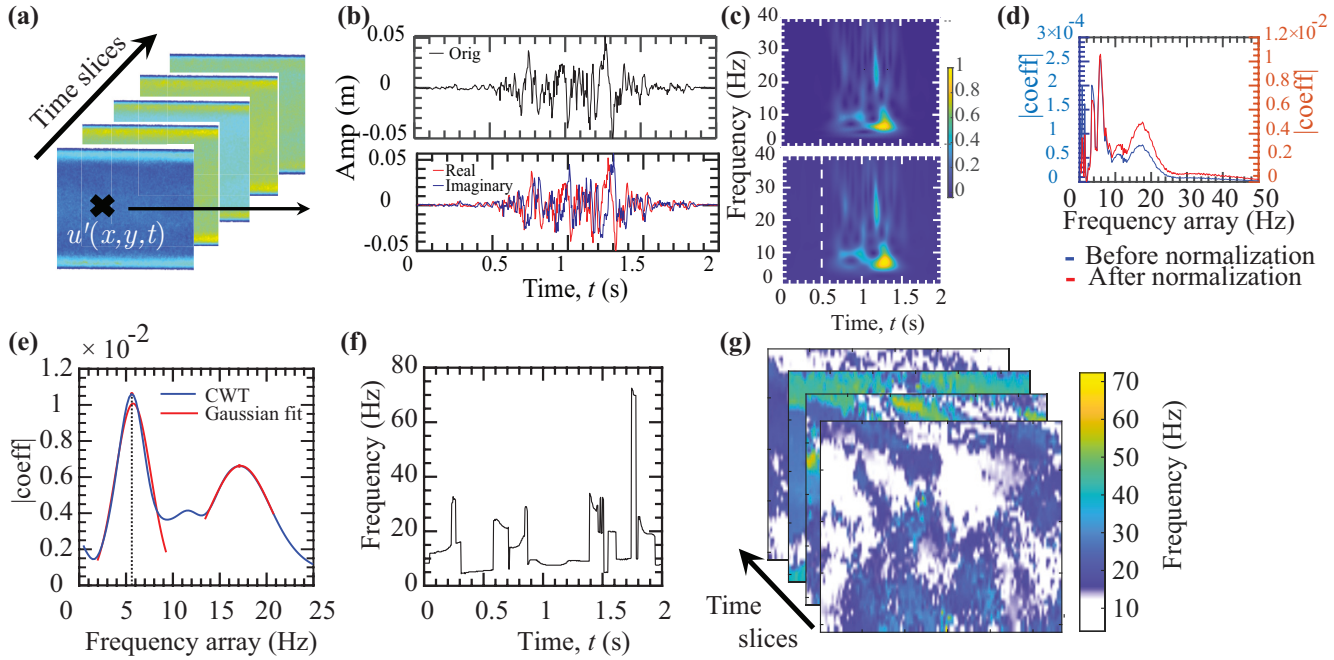

FIG. 1. Overview of the WHTF method. (a) The fluctuating velocity, u', array in time is extracted for a single spatial point. (b) The Hilbert transform of the "original" signal is computed and the (c) CWT coefficient map is evaluated (Top) and smoothed (Bottom) for this signal. CWT coefficients at each time step are extracted (see white dashed line in (c) Bottom) and (d) normalized to account for CWT peak differences across scales. (e) Peaks in the normalized coefficient array are identified and Gaussian fits are used to further localize the peak and identify the the dominant IF for that spatiotemporal point. This peak identification is repeated for all time steps. (f) The temporal variation of the dominant IF for the given spatial point. The process shown in (a)-(f) is repeated for all spatial points. (g) 2D spatial frequency maps showing the dominant IFs through space and time.

of the wavelet-coefficient field must be evaluated at each time step (i.e., each column of the wavelet coefficient map). Thus, each column of the wavelet coefficient field is iteratively extracted and evaluated individually, as represented by the dotted white line in Fig. 1(c) (Bottom).

Fig. 1(d) shows the extracted coefficient array at the time step of about 0.5s. The coefficient array is normalized using an empirically-defined normalization function in order to account for the uneven distribution of energy across scales inherent to the CWT. Specifically, an intrinsic drawback of the CWT is that low frequency components yield larger coefficient magnitudes than high frequency components, even when the two frequency components maintain the same amplitude. Fig. 2 explicitly demonstrates this, showing the CWT coefficient fields for one-frequency component sine signals with frequencies of 1 Hz, 50 Hz, and 100 Hz. It is clearly observed that the 100 Hz signal results in lower CWT coefficient magnitude than the 1 Hz or 50 Hz signals. Fig. 2(d) illustrates the peak CWT coefficient magnitude as a function of the sine signal frequency. The consequence of this inherent CWT limitation is that it creates a bias to select lower frequencies as dominant even in cases where a higher frequency has the same or even slightly higher

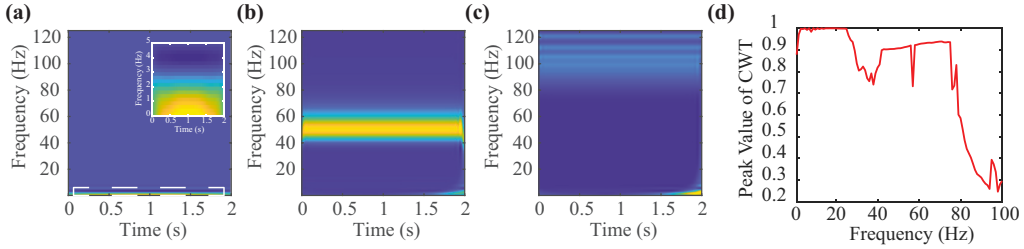

FIG. 2. Defining the scale-varying CWT normalization function. The CWT coefficient maps for sine signals with single frequencies of (a) 1 Hz, (b) 50Hz, (c) 100 Hz show the difference in CWT coefficient peak amplitude as a function of scale (frequency). The sub-tile in (a) zooms in on the low frequency range. (d) The peak CWT coefficient magnitude for sine signals with frequencies ranging from 1–100 Hz.

amplitude. Hence, for our purposes it is important to correct this behavior. Thus, we utilize the signal shown in Fig. 2(d) as the empirically-defined normalization function which is interpolated onto the CWT scales. Fig. 1(d) shows the CWT coefficient array after normalization, where it can be observed that low frequency peaks are reduced in magnitude and high frequency peaks are increased in magnitude.

Finally, the normalized coefficient array is smoothed using a moving average. The peaks of the normalized and smoothed coefficient array are identified in Fig. 1(e). A 15-point window around each peak is extracted and a Gaussian fit is evaluated on this window. The frequency corresponding to the peak of the Gaussian fit is computed. This Gaussian fit is used to account for any remaining noise and any scale-resolution limitations. The 15-point window size was chosen due as, through our testing, it showed high performance in aiding the selection of the best peak. However, one limitation of this 15-point window size is that it can lead to fit errors for smaller, less prominent peaks. Because here we are only extracting the most dominant peak, this limitation will not effect our results. However, the chosen window size should be reconsidered if multiple frequency peaks are to be considered or if a lower scale (i.e., frequency) resolution is used for the wavelet transform. Each evaluated frequency peak represents a frequency component in the signal at that time step. The dominant frequency is evaluated using a peak selection metric criterion. Specifically, peaks retained through the Gaussian fit are evaluated for peak prominence, peak height, and root mean square (RMS) error. The metric is computed as a ratio of the product of peak height and peak prominence to the square root of the RMS error. The peak with the maximum metric value is selected as the dominant peak. Iterating through each time step (each column of Fig. 1(c)) results in the 1D dominant frequency vs time array for the particular spatial point, as shown in Fig. 1(f). This entire process (steps (a)–(f)) is repeated for all spatial points in the flow field. Fig. 1(g) depicts the instantaneous dominant frequency evaluated at each spatial point and time, which is the output of the WHTF method.

Overall, the novelty of the WHTF method is the unique coupling of the established transforms, the wavelet coefficient normalization step, and the developed instantaneous peak detection. Using this approach, we overcome the limitations of the wavelet transform to deliver smooth and accurate instantaneous frequencies. The WHTF method was implemented in MATLAB®. Using a PC computer, and a typical experimental dataset of size 199 × 160 vectors with 1000 timesteps, the WHTF method calculates the dominant frequency for a single spatial point in approximately 1.5 seconds and takes about 13 hours for the entire dataset. While here we apply the WHTF method only to 2D datasets, its implementation is agnostic to the data dimensionality and thus the WHTF method can readily be applied as is to 3D data.

III. MATERIALS AND METHODS

A. Analytical Test Signals

1. Data generation

We first validated the accuracy of the WHTF method using 'single' and 'multi'-frequency analytical signals. Sine signals were generated according to: $A * sin(\omega t)$. Here, $\omega = 2\pi f$, where f is the ground-truth frequency and ω is the angular frequency of the signal. Amplitude, A, was kept at a constant value of 1. Each of these signals contained 499 data points and were defined for a duration of two seconds. The 'single'-frequency signals were defined such that only one frequency component, with variable frequency, existed in the signal at any given time. Specifically, each signal maintained one frequency from 0–1s and a different frequency from 1–2s. The signals were defined in this manner as one goal of this initial validation was to test the accuracy of the WHTF method for detecting step changes in frequencies. A total of 3 'single'-frequency signals were generated. For all signals, a frequency of 2Hz was used from 0–1s. From 1–2s, the frequency was varied across signals including values of 5 Hz, 50 Hz, and 100 Hz. 'Multi'-frequency signals were defined as the summation of two single-frequency sine functions. Each frequency was present through the entire signal. Three 'multi'-frequency signals were defined which used frequency pairs of 2 Hz + 5 Hz, 2 Hz + 15 Hz, and 2 Hz + 25 Hz. These pairs were selected to test the utility of WHTF to identify low frequency in addition to sensitivity of capturing another higher frequency above this low frequency.

2. State-of-the-art TF Methods used for Comparison Testing

The WHTF method was compared with other traditional methods of frequency estimation in the literature, including the short-time Fourier transform (STFT) and empirical mode decomposition-Hilbert Huang transform (EMD-HHT) [25]. The STFT was computed using the built-in MATLAB® function 'spectrogram' with a sampling window of 50 points. The window overlap was kept at 75% of the STFT window size. The number of points used for the fast Fourier transform (FFT) was kept at 500, (for signals with a sampling frequency of 250Hz). Through testing, these window size and overlap settings were determined to provide the highest accuracy for the STFT method for the tested signals.

The EMD-HHT was computed in two steps. First, the EMD was computed using the built-in MATLAB® function. The EMD output was used to compute the intrinsic mode functions (IMF) as described in Huang et al. [25]. The dominant frequency was then extracted as the first column output of EMD-HHT.

3. *Error Analysis*

Error analysis for the analytical signal testing was conducted to assess the accuracy of each tested TF method for estimating the ground-truth frequency. Here, the error was defined as the absolute error, i.e., the magnitude of the difference between the ground-truth frequency value and the value of frequency computed using the methods.

B. Experimental Datasets

Two experimental transitional pipe flow datasets, both captured using planar PIV were used for this study. One dataset included a suite of steady-mean flow test cases, which was specifically captured for this study. This dataset will be referred to as the "steady flow" dataset for the remainder of the manuscript. The second dataset included an unsteady-mean pulsatile flow test cases which were captured as part of a prior study by El-Khader and Brindise [30]. This dataset will be referred to as the "pulsatile flow" dataset for the remainder of the manuscript. Both datasets utilized the same experimental test rig. The Reynolds number for each dataset was defined using the equation provided in the Introduction. For the steady flow dataset, we refer to the Reynolds number as Re_s, while for the pulsatile flow dataset, we refer to it as Re_m. This distinction is made for completeness; however, Trip *et al.* [15] showed that pulsatile flows defined using their mean velocity maintained analogous TI vs. Re trends to steady-mean flows. Thus, Re_s and Re_m are expected to be effectively analogous such that side-by-side comparisons of the two datasets can validly be made.

1. *Steady Transitional Pipe Flow Dataset*

A schematic of the experimental flow loop and PIV setup used is shown in Fig. 3. The test section consisted of straight, rigid FEP (fluorinated ethylene propylene) tubing with an inner diameter, D, of 1/4". The test fluid, water (density, $\rho = 997kg/m^3$ and kinematic viscosity, $\nu = 0.98 \times 10^{-6}m^2/s$), was pumped through the loop using a computer-controlled gear pump. To monitor the flow loop, pressure transducers (Omega®) were placed upstream and downstream of the test section and an ultrasonic flowmeter (Transonic Inc.®) was placed upstream of the test section. The test section was preceded by a 150D+ length of uninterrupted tubing to ensure fully developed flow was captured. In addition, the test section was submerged in the working fluid (water)—which maintains the same refractive index (RI) as FEP—to reduce optical distortions in the PIV images. A total of 17 steady flow test cases

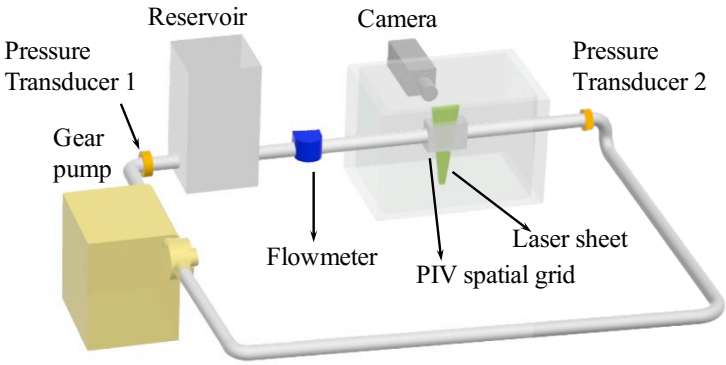

FIG. 3. Experimental setup used for the planar PIV experiments for both steady and pulsatile flows.

were captured. The steady flow Reynolds number, Re_s, for the measured cases ranged from 500-4500 to establish the onset of transition in our flow system. The complete list of test cases is provided in Table I.

A single 4-megapixel high speed camera (Phantom VEO®) was used to capture planar PIV images. An Nd-YLF(Neodymium-doped Yttrium Lithium Fluoride) laser (Photonic Industries®, $\lambda = 527$ nm) was used to create a laser sheet with a thickness <1 mm that was centered on the test section tube. The flow loop was seeded with 10 μm fluorescent particles. A double-pulsed PIV timing scheme was used. Image pairs (i.e., velocity fields) were captured at a frequency of 500 Hz. The inter-frame time of the camera was adjusted between cases such that the

TABLE I. POD parameters for steady flow test cases

Re_s	Effective dt (μs)	Modes	Energy retained (%)
500	225	1445	74.91
1000	113	1821	85.35
1500	75	1391	73.48
2000	56	1525	77.08
2100	54	3031	99.87
2200	51	1372	73.14
2300	49	1373	73.30
2400	47	3031	99.89
2500	45	3000	99.74
2600	43	3024	99.90
2700	41	141	62.73
2800	40	197	58.24
2900	39	197	49.85
3000	38	244	52.09
3200	35	240	49.91
3500	32	283	50.80
4500	25	422	56.04

maximum particle displacement per frame was around 8-12 pixels. Table I reports the inter-frame time for all cases. The camera magnification was 4.15 μm/pixel. The image resolution was 2560×1600 pixels and a total of 1000 images were captured for each test case.

PIV images were processed using a publicly available software Prana. Processing was done using three passes of an iterative image deformation algorithm, and robust phase correlation (RPC) [41–43]. A window size of 64×64 with a 50% Gaussian window was used for the final pass. This resulted in a 32×32 pixel effective window size which mitigated spectral leakage. The PIV final pass used an 8×8 pixel grid size. The velocity fields output from the final PIV pass were of size 199×160 vectors.

PIV velocity fields for the steady flow data were post-processed first using universal outlier detection (UOD) to remove spurious vectors [44]. Specifically, three-passes of a median-based UOD were used which included a window size of 7×7 and threshold of 3, a window size of 5×5 and threshold of 2, and a window size of 3×3 and threshold of 2. Subsequently, proper orthogonal decomposition (POD) was applied to the velocity fields. POD decomposes the velocity fields into a set of eigenmodes; a subset of these modes are reconstructed to yield a reduced-order, smoothed version of the velocity field data. The number of modes retained for the reduced-order reconstruction were autonomously calculated using the entropy line fit (ELF) thresholding criterion, as shown in Brindise and Vlachos [45]. The resultant filtered velocity fields were used for all post-processing calculations. To confirm the accuracy of the PIV data, we compared the experimental velocity profile for the $Re_s = 500$ case, which is well within the laminar regime, to the analytical Poiseuille flow profile. The error was found to 1.5%, highlighting that the PIV study was well-controlled and accurate.

2. *Pulsatile Transitional Pipe Flow Dataset*

The pulsatile transitional pipe flow dataset from El-Khader and Brindise [30] was used herein. We provide a brief description of this dataset, but the refer the reader to El-Khader and Brindise [30] for complete details.

A total of 12 test cases from the prior study were analyzed for this work. These included mean Reynolds number (Re_m) values of 800, 2300, 2500, 2700, 3200 and 4200, each at two Womersley numbers of 4 and 12, defined by, α ($= R\sqrt{(2\pi f/\nu)}$), where R is the radius of the pipe and ν is the kinematic viscosity. We note that 6 additional test cases were captured as part of the El-Khader and Brindise [30] study; these included Womersley numbers of 6, 8, and 10, each captured at Re_m of 2500 and 2700. However, these test cases were not included herein. The literature has shown that the flow behavior is altered for Womersley numbers $\geq$ 10, as compared to Womersley numbers l 10 [46, 47]. Thus, the Womersley number values of 4 and 12, alone, should sufficiently capture a broad range of pulsatile flow dynamics.

The flow loop design for the pulsatile flow dataset matched that of the steady flow dataset collected for this study. The same test section, camera, and laser sheet configuration were used. For this study, the camera magnification was set at 6.67μm/pixel and images of size 1024×1024 pixels were captured. The PIV images were collected using a double-pulsed timing scheme. Image frame pairs were captured at 750 Hz, and the inter-frame time between images in the pair was adjusted between cases to ensure a maximum particle displacement of 8-12 pixels. The frame pair frequency was set to ensure at least two pulsatile cycles were captured for each test case. PIV images were processed

using the same protocol as used for the steady flow data. Velocity fields for the pulsatile flow cases were of size 127×127 vectors.

The velocity fields for the pulsatile flow were post processed using POD first. ELF was again employed to determine the modes to retain. After this, UOD analysis was done to remove any outliers in the data, which were particularly possible around the edges of the spatial grid. The post-processed velocity fields for the pulsatile flow data for UOD settings were similar to steady flow. Finally, the velocity fields were phase-averaged using 2 pulsatile cycles. The smoothed and phase-averaged velocity fields were used for all subsequent calculations.

3. Post-processing

For both datasets, the fluctuating velocity components (u' and v') were first computed using the Reynolds decomposition. For the steady flow data, the fluctuating velocity fields were obtained after subtracting the temporal mean velocity from the post-processed velocity components. As, the steady flow is time independent, the mean velocity was just computed as a simple averaging. For the pulsatile flow data, the fluctuating velocity components computed in El-Khader and Brindise [30] were used as is. Briefly, the mean velocity calculation for this dataset needed to account for the pulsatility and not enough pulsatile cycles were computed to utilize a traditional ensemble averaging. Thus, as done in Brindise and Vlachos [48], the mean velocity components were calculated as a fifth-level DWT decomposition of the one-dimensional temporal velocity field at each spatial point using a 'sym8' wavelet. This calculation removes high-frequency components, leaving only the underlying low-frequency pulsatile waveform. This calculation is repeated for each spatial point to compute the mean velocity components for the entire dataset.

Turbulent kinetic energy (TKE) and TI were subsequently computed according to Eqn. 1 and Eqn. 2, respectively, where $\overline{U}$ is the centerline velocity.

$$\mathrm{TKE} = \frac{1}{2}(u'^2 + v'^2), \tag{1}$$

$$\mathrm{TI} = \frac{1}{\overline{U}}\sqrt{\frac{1}{2}(u'^2 + v'^2)}, \tag{2}$$

Because the datasets are captured in a two-dimensional, two-velocity component (2D-2C) manner using planar PIV, Eqn. 1 and Eqn. 2 do not include the third-dimensional w' component since it is not measured by this setup. The use of a 2D data capture is an apparent limitation of this study. However, we note that for shear flows, employing Squire's theorem, it suffices to study the cause of a 2D flow being unstable since, if a 2D flow is unstable then consequently, the 3D flow will be unstable.

4. Details on TF-based metric evaluations

The WHTF was evaluated for each test case. Using this output, dominant frequencies could be plotted as instantaneous 2D spatial contour maps (i.e., as shown in Fig. 1(g)). Using this mapping, so-called "coherent frequency structures", which are connected regions in the spatial grid having similar frequencies, were evaluated. To do this, the built-in MATLAB® function *imbinarize* was first applied to the spatial frequency map contour to identify the connected frequency regions. Adjacent spatial grid locations were considered connected if their frequency values were within 0.4 Hz. Using the frequency contours, the number of contours as well as mean frequency and area of each contour could be directly computed.

The Shannon entropy of the discrete cosine transform (DCT) of the 2D spatial frequency maps were computed to quantitatively estimate the overall coherence of the maps. The DCT-entropy metric was introduced by Brindise and Vlachos [45] and shown to accurately estimate the coherence vs. speckled-nature of a 2D map. For this calculation, the 2D DCT of the 2D spatial frequency maps were computed. The Shannon entropy of these DCT maps were subsequently calculated.

Joy Kolliyil *et al.* [22] highlighted that evaluating the instantaneous frequency of the TKE could be used to decompose the Kolmogorov spectrum. Thus, herein, we evaluated how the instantaneous frequency spectrum changed across different flow regimes. For this analysis, TKE histograms were computed at each time step at each scale. We refer the reader to Joy Kolliyil *et al.* [22] for complete details on this calculation. Briefly, in the 2D spatial map, the instantaneous frequency and TKE value pairs are considered. For each unique frequency value, the corresponding TKE values for all spatiotemporal points with that frequency are summed (effectively a histogram). Hence, a total TKE vs. frequency distribution is computed.

IV. RESULTS AND DISCUSSION

A. TF method comparison using analytical signal suite

We first analyze the accuracy and rigor of the WHTF method as compared to traditional TF analysis methods (STFT and EMD-HHT) using the analytical signal suite with known ground-truth frequencies. Fig. 4(a)–(c) shows the frequencies estimated by each TF method for the three single-frequency analytical signals, while Fig. 4(d)–(f) shows the corresponding error analysis.

A significant ringing effect for the EMD-HHT is clearly observed. The oscillations worsened as the magnitude of the analytical frequency jump occurring at 1s was increased. This behavior is analogous to the ringing effect often observed with fast Fourier transforms (FFTs). The STFT exhibited no oscillatory behavior for high frequencies. However, for low frequencies—the 2Hz frequency especially and less so the 5Hz frequency—oscillations at the estimated frequency were observed. Here, this is a result of resolution limitations inherent to the STFT. Specifically, for lower frequencies, the window size is too small to accurately detect the frequency. With the WHTF method, little to no oscillatory behavior in the estimated frequency trend was observed. However, the WHTF did suffer from, at times, bias errors in the predictions. For example, in Fig. 4(c), from 1–2s when the analytical frequency was 100 Hz, the WHTF predicted the frequency to be 104 Hz, a 4% bias error. Because the WHTF utilizes the CWT, this error occurs as a result of inherent limitations of the wavelet transform. Specifically, at high frequencies, the CWT maintains a low resolution in frequency; this produces a broad CWT coefficient peak, leading to higher uncertainty in the predicted frequency value. In Fig. 4(c), the WHTF also exhibited a time-delayed recognition of the frequency change at 1s. This occurs because the previously discussed limitation that CWT favors low frequency peaks that results in a delay of when the high frequency peak achieves a higher amplitude than the low-frequency peak.

Table II summarizes the errors associated with each TF method for the single-frequency signals. For the 5 Hz and 50 Hz signals, the WHTF maintained on average a 63% and 45% improvement over the EMD-HHT and STFT methods, respectively. For the 100 Hz signal case, the WHTF maintained a high mean error. However, this error decreases to 2.42 ± 5.00 Hz when the delayed detection of the frequency change and edge effects are excluded. Nonetheless, the STFT method maintained the best performance for this high-frequency case.

Fig. 5 considers the performance of each TF method when more than one frequency is present throughout the signal. For this analysis, it is particularly of interest to evaluate which frequency is detected by each TF method and to what extent the predicted frequency jumps between the two possible solutions. For all signal pairs, the STFT identified only the larger of the two frequencies as the dominant frequency and did not detect the lower 2Hz component. This can be attributed to window resolution limitations, which cause the STFT to favor larger frequencies. The EMD-HHT method similarly identified the higher frequency for all signal pairs. However, the EMD-HHT again maintained considerable oscillations throughout as well as large errors at the start and end of the signal. The WHTF method

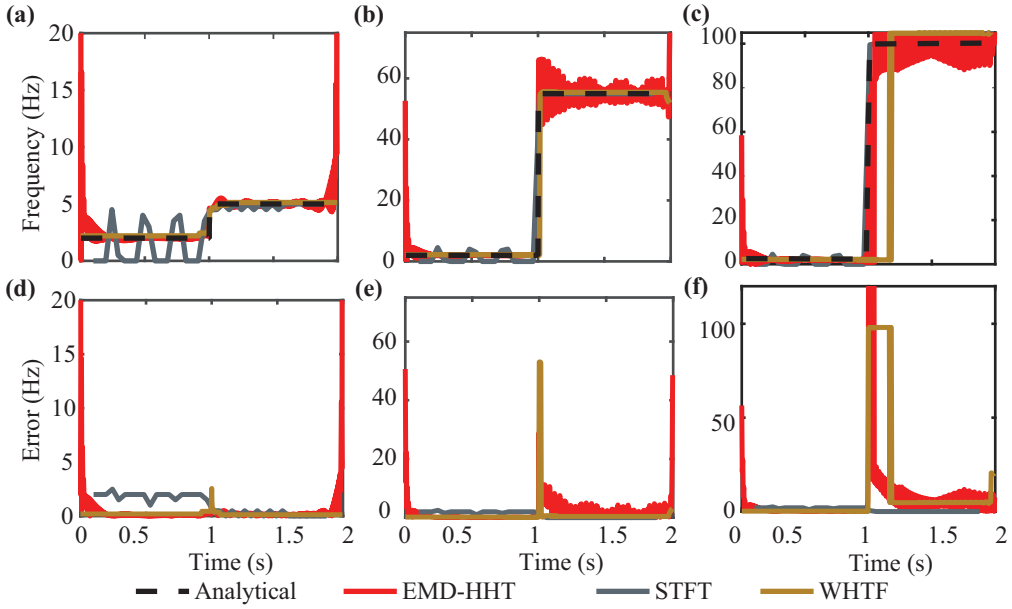

FIG. 4. Frequencies identified by the EMD-HHT, STFT, and WHTF methods for the single frequency signals with a 2 Hz frequency from 0–1s and a frequency from 1–2s of (a) 5 Hz, (b) 50 Hz, and (c) 100 Hz. (d-f) show the error associated with each time-frequency method for the 2 Hz to 5 Hz, 2 Hz to 50 Hz, and 2 Hz to 100 Hz signals, respectively.

TABLE II. Comparison of WHTF, STFT and EMD-HHT for the three single frequency signals. The values are reported as mean ± standard deviation.

Cases	WHTF	STFT	EMD-HHT
2 & 5 Hz	0.18 ± 9.14	1.03 ± 0.13	0.52 ± 3.20
2 & 50 Hz	0.88 ± 4.25	0.96 ± 0.99	2.24 ± 4.38
2 & 100 Hz	11.12 ± 27.53	0.97 ± 0.98	6.27 ± 22.08

maintained the most varied selection of the dominant frequency component. In Fig. 5(a), for the 2 Hz + 5 Hz frequency pair, the WHTF method only identified the 5 Hz signal. Conversely, for the highest frequency pair case of 2 Hz + 100 Hz (Fig. 5(c)), the WHTF identifies the low-frequency as the dominant peak. The 100 Hz is only selected as dominant for the very beginning and end of the signal. This can be attributed to resolution limitations arising from edge effects of the CWT mapping. For the 2 Hz + 50 Hz case (Fig. 5(b)), the WHTF selects the lower frequency as dominant in the middle of the signal (0.5s–1.5s), but the 50Hz component as dominant outside of this window. The variable dominant frequency selection can be attributed to the peak selection on the basis of coefficient magnitude coupled with the inherent limitation that CWT coefficient magnitude is frequency-dependent. In general, this multi-frequency signal analysis demonstrates that the WHTF method is the only method capable of identifying low-frequency components when high-frequency components are present. This, combined with its improved accuracy for frequency detection, makes the WHTF method most suitable for analyzing instantaneous frequency components in flow velocity fields.

Fig. 5(d)–(f) show the CWT coefficient maps for multi-frequency signals. It is clearly observed that both frequency components are identified by the CWT, but because only one frequency is selected by the peak detection, one frequency component is defacto missed by the WHTF method. While adding a second peak identification to the WHTF method can resolve this issue, adding this capability is not desirable for the goals of this work. Specifically, this is because Joy Kolliyil *et al.* [22] demonstrated that for noisy signals only the most dominant frequency can be accurately identified, even when additional signal windowing modules are included to improve frequency identification. Furthermore, Joy Kolliyil *et al.* [22] highlighted that the turbulent behavior of a flow is often contained within a single IF, such that the WHTF should be capable of providing critical details regarding transition progression. Hence, identifying a single dominant frequency is the first step towards arriving at a universal metric which can successfully predict this transition. Nonetheless, expanding the WHTF method to extract multiple instantaneous frequencies should be explored in future work. The primary challenge of this expansion is that it will increase the dimension of the data analysis.

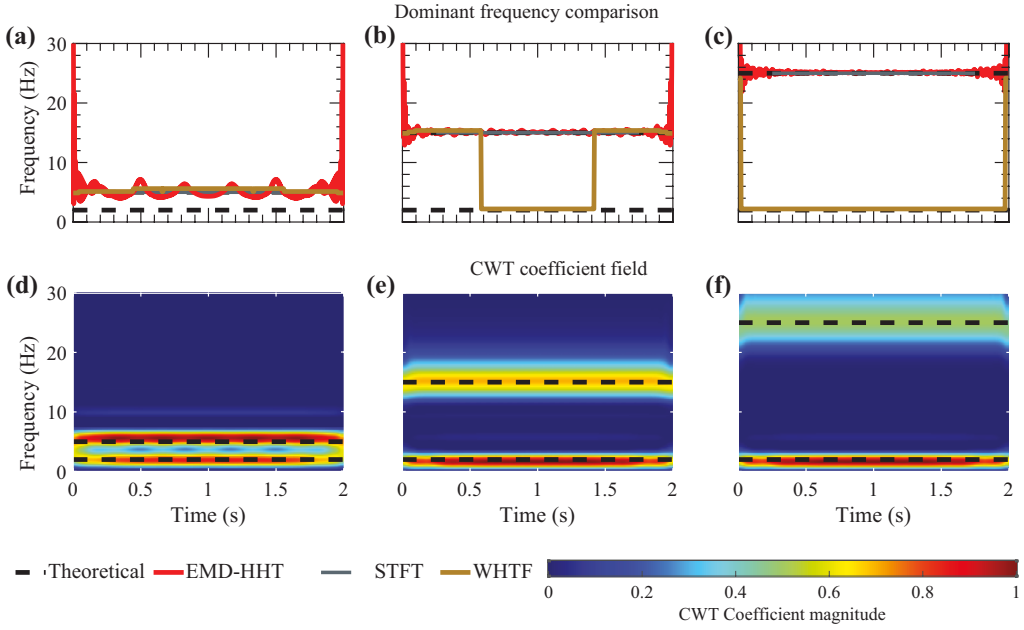

FIG. 5. Frequencies identified by the EMD-HHT, STFT, and WHTF methods for the two frequency (a) 2 Hz + 5 Hz, (b) 2 Hz + 50 Hz, and (c) 2 Hz + 100 Hz signals. (d)-(f) show the CWT coefficient field computed by the WHTF method for the 2 Hz + 5 Hz, 2 Hz + 50 Hz, and 2 Hz + 100 Hz signals, respectively.

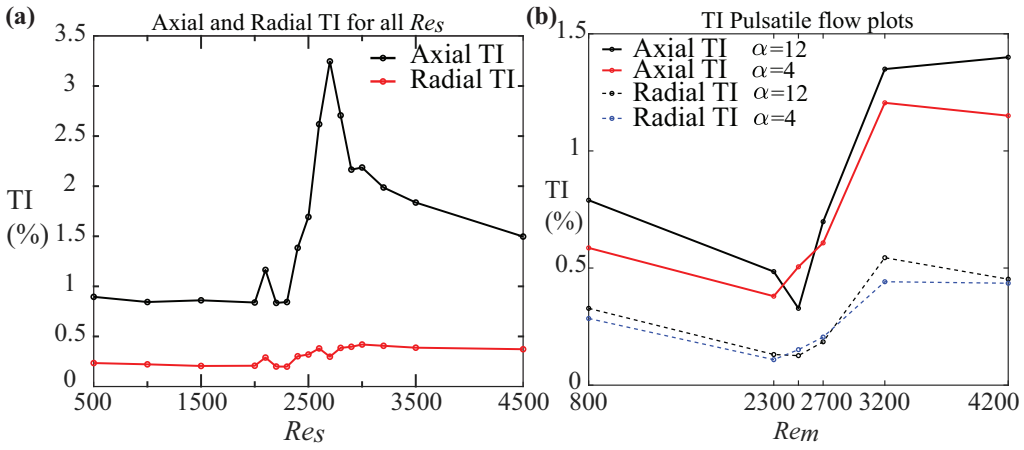

FIG. 6. Turbulence intensity (TI) vs Reynolds number for (a) the steady flow dataset and (b) the pulsatile flow dataset including Womersley numbers 4 and 12.

B. Characterizing transition for our experimental setup

Next, the onset of transition as well as the critical Reynolds number for the steady experimental dataset are characterized. This information will serve as a ground-truth by which the efficacy of TF-based metrics to evaluate transition progression.

To evaluate the onset of transitional and fully turbulent flow, the traditional TI vs Re (S-shaped) curve was used. Fig. 6(a) shows the axial and radial TIs vs Re_s for the steady flow dataset. The observed curves closely matches those reported by Trip et al. [15], albeit with a slight shift of the $Re_{critical}$ value. For our setup, the onset of transition is seen at a Re_s of 2400, which is the point where the axial TI begins to rapidly increase. The $Re_{critical}$ is typically marked as the point where the axial TI begins to level off and/or where the radial TI S-curve plateaus. For our setup, this occurs at an $Re_s = 3000$. As the flow regime becomes fully turbulent, the axial TI decreases slightly with increasing Re_s, while the radial TI is plateaued and remains at a constant value. The peaks and valleys correspond to sub-critical transition as the flow in the laminar regime is largely 2D and gets disturbed to evolve to transition and eventual turbulence. The momentary fluctuation seen at $Re_s = 2100$ in Fig. 6(a) is most likely the effect of ancillary experimental disturbances which subsequently get relaminarized locally.

For the pulsatile flow data, the exact critical Re_m could not be ascertained as the data did not maintain a high enough resolution for tested Re_m values within the transitional regime. Nonetheless, estimates for the onset of transitional and fully turbulent flow can be observed in Fig. 6(b). Specifically, for both Womersley numbers, transition begins around a Re_m of 2300 and full turbulence is achieved by a mean Re_m of 3200. This aligns with the findings of Trip *et al.* [15] who found that steady flow and pulsatile flows with Womersley numbers greater than 10 maintained negligible differences in the critical Re_m values. The axial and radial TI behavior was consistent across both values of α. Specifically, a gradual decrease in both axial and radial TI occurred in the laminar regime until the Re_m reaches the onset of transition. Beyond this point, the TI trends increased with increasing mean Re, until turbulence was achieved, at which point the trends roughly plateau. Hence, despite the similarity of critical $Re's$ across the steady and pulsatile datasets used here, notable differences in the behavior of the axial and radial TI trends were observed. For example, the axial and radial TI trends were largely similar for the pulsatile flow data, a finding inconsistent with the steady flow data. The different TI trends in pulsatile flow as compared to steady flow suggests underlying differences in the flow dynamics exist [49]. Hence, this finding implies that the unsteady component in the pulsatile flow effects the development of transitional and turbulent flow, but does not alter the critical Re. Ultimately, this demonstrates that the two datasets (steady and pulsatile) provide a robust set for our evaluation of TF-based metrics to assess transition progression in flow environments with varying turbulence development dynamics.

C. Evaluating TF-based metrics capable of characterizing transition progression

With the onset of transition and turbulent flow identified for our two test datasets, we next evaluated how the instantaneous frequency structures changed through the laminar, transitional, and turbulent regimes in order to determine the extent to which these features can be used to characterize transition progression. Fig. 7 plots the temporally-averaged spatial frequency map for the steady flow dataset at Re_s values ranging from 2200 to 3500. Here, the temporal averaging was done by averaging the instantaneous (i.e., at one time point) 2D spatial frequency maps through the entire time span of the data.

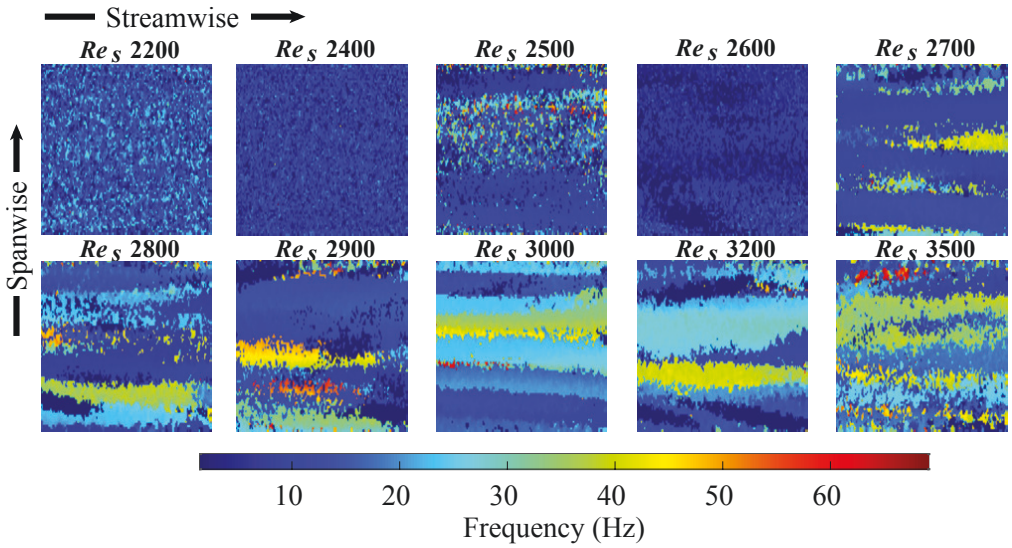

FIG. 7. Montage of frequency spatial structures within the pipe for varying Re_s values ranging from 2200–3500.

Hence, for each tile shown in Fig. 7, the streamwise (i.e., axial) direction varies from left to right and the spanwise (i.e., radial) direction varies from top to bottom. In the laminar regime (Re_s values of 2200 and 2400), fine frequency structures with an average frequency of 28 Hz are present throughout the pipe, which present with no general coherence. As the Re_s increases through the transitional regime (2500 to 2900), frequency structures with increasing coherence are observed. The frequency structures are primarily narrow-banded, axial in nature, and maintain a frequency of 25–45 Hz. Outside of these coherent frequencies, the remainder of the pipe generally maintains a baseline frequency of about 15 Hz. Once the flow achieves full turbulence at an Re_s of 3000, the coherent frequency structures primarily span the pipe cross-section, with minimal area maintaining a background frequency value. In the well established laminar regime, the fluid motion is dictated by movements of fluid layers which translate on top of each other [50]. This likely results in the frequency of the flow to be similar across the pipe cross section for laminar flow. However, as the flow starts evolving to the transitional regime, these layers are disturbed due to various factors such as increased friction and as a result the frequency composition changes in the radial (spanwise) direction. This causes locations in the pipe to have higher and lower frequencies based on relative motion. While the individual contribution of pressure and inertial forces on the frequency computation cannot be explicitly determined herein, it is of interest to evaluate in order to decompose the transition dynamics more explicitly. Thus, further studies which can correlate the velocity and pressure gradients with frequency gradients in 3D should be explored.

Fig. 7 confirms that the dominant instantaneous frequency does change based on flow regime. Several specific, notable differences in the frequency structures were observed in the laminar, transitional, and turbulent regimes. In particular, the background frequency value, the area of the frequency structures, and the coherence of the frequency structures were markedly different for each flow regime. Thus, each of these represent possible metrics capable of characterizing the progression of transition.

Fig. 8 plots the 1D spatial averaged frequency across the centerline of the pipe, which explores the background frequency notion. For the steady flow data, in Fig. 8(a), the centerline frequency was constant in the laminar regime, with a frequency value of about 29 Hz. As the flow becomes transitional (shown in gray), the centerline frequency plummets to a frequency of about 17 Hz at $Re_s = 2600$. This low centerline frequency can be observed in Fig. 7 as well, where the $Re_s = 2600$ case maintained very low frequency values throughout the pipe. For the later-stage transitional regime and early turbulent regime (Re_s between 2600 and 3500), the centerline frequency recovers to about 27 Hz, before decreasing to about 23 Hz by an $Re_s = 4500$. A somewhat similar behavior was observed for the centerline frequency trend in the pulsatile flow datasets, as shown in Fig. 8(b). For this case, the frequency was around 40 Hz for $\alpha = 4$ and around 42 Hz for $\alpha = 12$ in the laminar regime. In the transitional regime, the lowest frequency was around 30 Hz, beyond which the frequency behavior differed for each value of α. For $\alpha = 4$, the frequency recovered in the turbulent regime to 36 Hz. However, for $\alpha = 12$, the frequency dropped further to 28 Hz. This likely occurs as a result of the fact that changes in flow dynamics occur for flows with $\alpha >$10. Specifically, prior studies have highlighted that for $\alpha > 10$, transition dynamics mimic steady flow whereas for flow with $\alpha < 10$, the transition dynamics are influenced by the pulsatile phase [30]. Overall, for pulsatile flow, the drop of centerline frequency magnitude as the flow became transitional was not as significant as compared to that of steady flow. Specifically, a 16 Hz drop occurred in the steady flow, while only a 10 Hz drop occurred in the pulsatile flow. Additionally, the pulsatile cases maintained

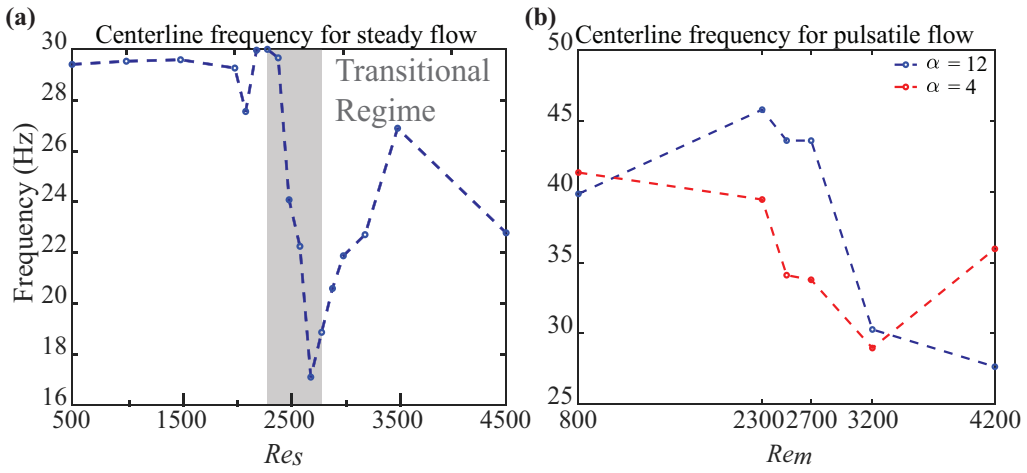

FIG. 8. Centerline frequency vs Reynolds number for the (a) steady flow dataset (where the transitional flow regime is shown in gray) and (b) pulsatile flow datasets.

about a 10 Hz higher frequency magnitude across all Re_m values as compared to the steady flow data. The laminar to turbulent peak frequency difference for steady flow was about 6 Hz as opposed to 3 Hz and 10 Hz for the pulsatile cases corresponding to $\alpha = 4$ and $\alpha = 12$, respectively. These results highlight that the centerline frequency does demonstrate a trend that notably differentiates the laminar, transitional, and turbulent regimes for both datasets. However, because of the frequency magnitude value differences, the metric—in its current, dimensional form—does not provide a means to determine the level of transitional or turbulent flow given a single representation (i.e., one Re value) of a specific flow. It is plausible that an appropriate non-dimensionalization of the centerline frequency could provide a universal metric to this end. Evaluating this notion would require additional standalone datasets and hence this should be explored in future work.

Fig. 9(a) plots the average area of the frequency spatial structures as a function of Re_s for the steady flow dataset. The mean size of the area structures were about 0.005 mm^2 for the laminar regime. As the flow evolved to the transitional regime, the mean area jumped to 0.012 mm^2 at $Re_s = 2800$, and stabilized at a mean area of about 0.01 mm^2 at the $Re_{critical}$ of 3000. In the turbulent regime, the mean area structures decreased to about 0.008 mm^2. Fig. 9(b) shows the mean area structures for the pulsatile flow datasets. Similar to the steady flow dataset, the area magnitudes remained constant in the laminar regime for both Womersley numbers. However, the behavior in transitional and turbulent regimes differed. For $\alpha = 4$, the mean area increased steadily throughout the transitional and turbulent regimes. Conversely, for $\alpha = 12$, the mean area jumped to about 0.022 mm^2 between the mean Re values of 2700 and 3200, and remained plateaued at this value through the turbulent regime. Together, Fig. 9(a) and 9(b) suggest that the development of transition occurs faster in the steady and steady-mimicking $\alpha = 12$ flows, and more gradually in the $\alpha = 4$ flow. Overall, the mean area of frequency structures was universally observed to increase from the laminar to the turbulent regime.

Fig. 9(c) and 9(d) show the area fraction (ϕ_s and ϕ_m) as a function of Re for the steady and pulsatile flows, respectively. Area fraction is a dimensionless quantity computed as the ratio of the total area within coherent frequency spatial structures to the total area of the pipe section. The 'total area within coherent frequency spatial structures' is defined using two thresholds. First, only areas whose frequency value is greater than the mean frequency of the flow are included. This threshold enables the extraction of features having higher frequency makeup capable of influencing the flow dynamics. Second, an area size threshold is applied to include only areas of 20 sq. pixels or greater. This value is chosen anywhere below the median values so that any variations beyond such a small magnitude is insignificant. For both the steady and pulsatile flows, the area fraction increased slightly through the laminar regime within the range of 0.38–0.43. For the steady flow dataset, area fraction began decreasing at an Re_s of 2000. This decrease occurred throughout the transitional regime, before leveling off at an area fraction of about 0.35 in the turbulent regime. For the $\alpha = 4$ case, area fraction began decreasing at an Re_m of 2400, bottoming out at 0.35 at an Re_m of 3200, and then finally increasing to about 0.37 in the turbulent regime. For the $\alpha = 12$ case, area fraction decreased sharply from an Re_m of 2700 to 3200 (dropping from 0.40 to 0.36), and then recovered to about 0.385 at an Re_m of 4200. Thus, for all flow the turbulent regime area fraction recovered to roughly that of the laminar regime, while the area fraction dropped in the transitional regime. However, Fig. 9(a) and 9(b) highlighted that the overall size of the areas in the flow increased in transition. Hence, the area fraction analysis suggests that the slugs and puffs forming in the transitional regime maintained low frequencies, below the mean flow frequency. Overall, the area and area fraction do demonstrate a relationship with turbulence progression, but similar to the centerline frequency

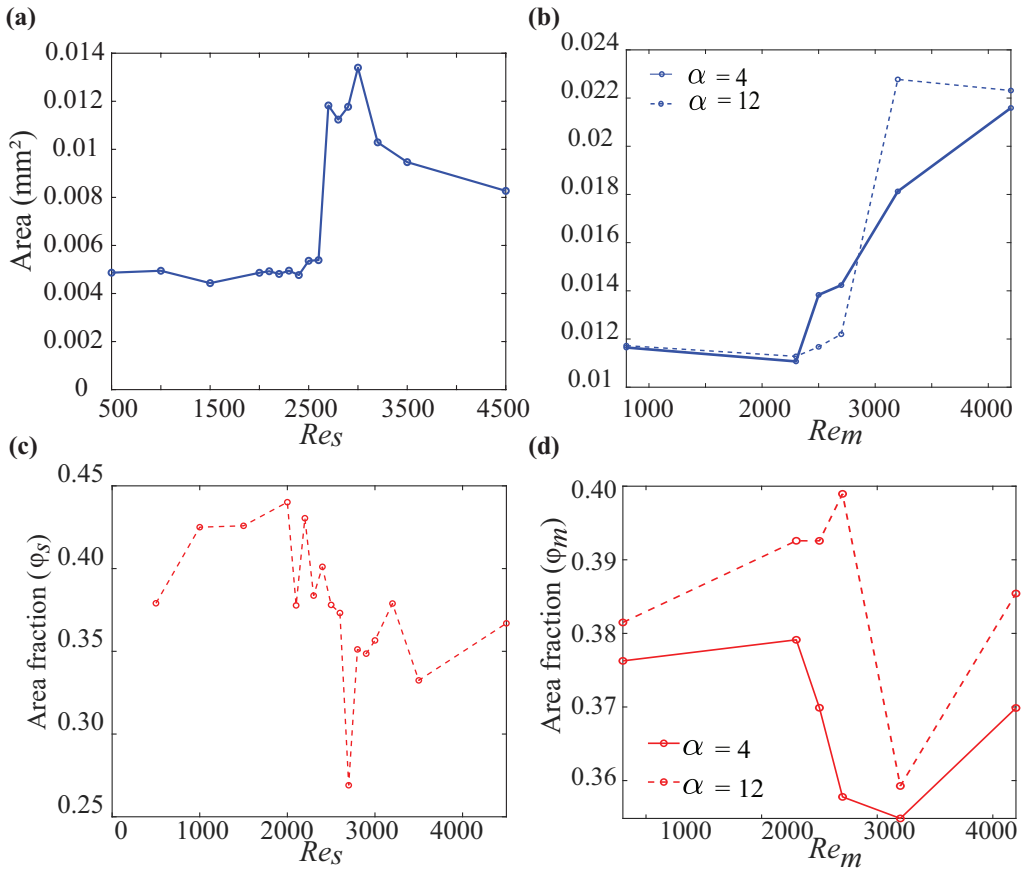

FIG. 9. Mean area (in mm^2) of spatial frequency structures for (a) steady flow and (b) pulsatile flow datasets. Area fraction (ϕ_s) as a function of Reynolds number for (c) steady flow and (d) pulsatile flow datasets.

analysis, a scaling or bias difference between the steady and pulsatile values existed.

Fig. 10 shows the histograms for laminar, transitional, and turbulent regime Re values for the steady and pulsatile datasets. For the steady flow (Fig. 10(a)), the most prevalent area size for the laminar regime was approximately 0.0005 mm^2. This increased to 0.008 mm^2 as the flow became turbulent. Fig. 10(b) and 10(c) show the histograms for the pulsatile flow dataset of $\alpha = 4$ and $\alpha = 12$, respectively. The most prevalent area size for the laminar regime was about 0.0005 mm^2 and 0.0001 mm^2 for the 4 and 12 Womersley number cases, respectively. In the turbulent regime, these values increased to 0.001 mm^2 for $\alpha = 4$ and 0.002 mm^2 for $\alpha = 12$. A notable difference in the total number of structures was observed, where the $\alpha = 4$ case maintained about 4 times more structures than the steady flow case and about 5 times more structures than the $\alpha = 12$ case. This difference likely indicates that for the $\alpha = 4$ case, where pulsatility-induced structures have sufficient time to develop, leads to a significant increase in frequency structures. Despite the change in the number of spatial structures, the distribution of spatial structures appears to be unimodal and generally consistent for all cases. As the Reynolds number increased, an increase in the number of large area structures is clearly observed for all flows. Furthermore, in the turbulent regime, the decrease in the number of area structures becomes more gradual. Both of these findings indicate that the coherent frequency structures generated by turbulent flow are larger in spatial area than for laminar flow. Hence, this suggests that this characteristic of peak area magnitude does reflect the progression of transitional and turbulent flow development. However, further analysis is required to comment and classify this distribution as a type of log normal. Additionally, future studies should aim to correlate the skewness of such a distribution to the effect of Womersley number on the peak of these area structures.

Fig. 11 evaluates the coherence of the frequency structures through the laminar, turbulent, and transitional regimes. Specifically, the DCT-entropy of the 2D spatial frequency maps shown in Fig. 11 are evaluated; DCT-entropy has been shown to provide a representative estimate of the organization of structures in a given flow field (or 2D map in general) [45]. Here, a higher DCT-entropy is expected to correlate with increased coherence of frequency structures. S-curve-type trends of the DCT-entropy are observed for both the steady and pulsatile datasets. In the laminar regime, the steady flow case, maintained an average DCT-entropy of 0.10, while the pulsatile flow with $\alpha = 4$ and $\alpha = 12$ had DCT-entropy values of about 0.08 and 0.30, respectively. The DCT-entropy increased significantly in the

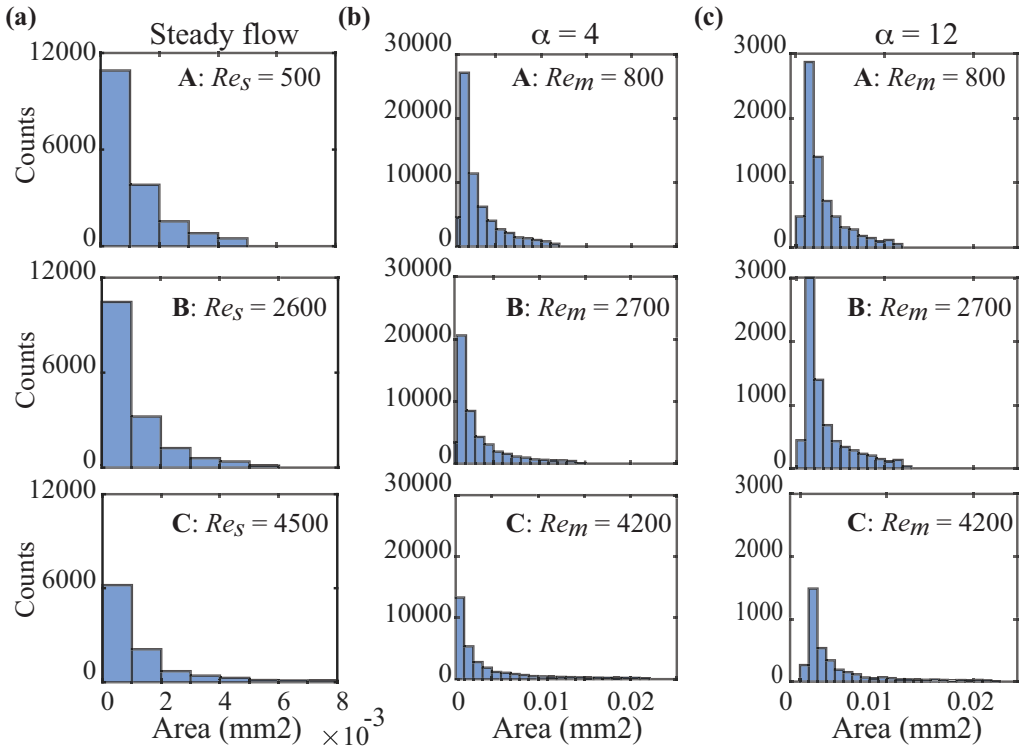

FIG. 10. Distribution of area histograms for one laminar, one transitional, and one turbulent regime case in (a) steady flow, (b)-(c) pulsatile flow for $\alpha = 4$ and $\alpha = 12$, respectively. The bin width is kept constant across all cases at 0.001 mm^2.

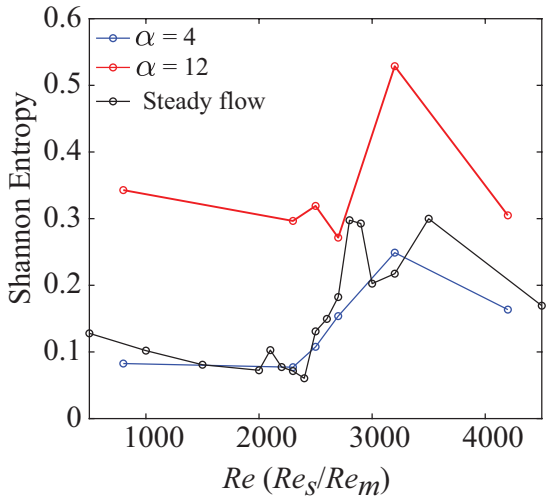

FIG. 11. DCT-entropy for steady flow and pulsatile flow datasets including both the 4 and 12 Womersley numbers (α).

transitional regime, peaking at 0.30 for the steady flow data, 0.27 for the pulsatile flow data with $\alpha = 4$, and 0.55 for the pulsatile flow data with $\alpha = 12$. In the turbulent regime, the DCT-entropy decreases somewhat to about 0.18 for both the steady flow and pulsatile $\alpha = 4$ cases and to 0.30 for the pulsatile $\alpha = 12$ case. In general, the DCT-entropy trends for the steady and pulsatile flow, $\alpha = 4$, are strikingly similar both in terms of trend and magnitude, while for the $\alpha = 12$ case, the trend is similar, but magnitude is higher. This finding is of particular interest given that the $\alpha = 12$ case is expected to be steady-mimicking, yet the DCT-entropy trend suggests the opposite behavior. One possible explanation for this finding is that the high-frequency pulsation associated with the 12 Womersley number flow does serve to increase the overall energy in the flow, leading to a higher entropy. Considering Fig. 11 and Fig. 7, our findings suggest that in laminar flow, where no flow scales are expected, no frequency components truly exist within the flow. Hence, the lower values of DCT entropy in the laminar regime most likely reflect the pump fluctuations

and other experimental artifacts which are captured by the frequency algorithm. In the transitional regime, however, DCT entropy values peak. This likely occurs as a result of the rapid generation and dissipation of identifiable slugs and puffs which disturb the flow and generate clear and frequency components in the flow. In turbulent flow, the slugs and puffs are produced at higher rate than in transitional flow such that they are no longer individually discernible and maintain an "interference" with one another. This would be expected to reduce the coherence of the frequency structures and provide an explanation for the reduced DCT-entropy in the turbulent regime.

Fig. 12(a) shows the total TKE vs. frequency line and demonstrates the fitted -5/3 slope Kolmogorov spectrum line on a log-log scale for the steady flow at $Re_s = 4500$ case. The upper and lower frequency bounds between which the total TKE line matches the Kolmogorov spectrum were identified. This was done by extracting the abscissa value at the ends of this line segment.

Fig. 12(b) and 12(c) show the time-averaged upper and lower TKE spectral bounds for all the steady flow and pulsatile flow cases, respectively. For the steady flow, laminar regime ($Re_s < 2000$), the total TKE-frequency trend matched the Kolmogorov spectrum for frequencies of about 30–50 Hz. By the transitional regime, this frequency range expands to about 10–70 Hz and in the turbulent regime, the frequency range reduces to about 10–40 Hz. Hence, this suggests that the laminar regime maintains a higher frequency range, the turbulent regime corresponds to a lower frequency regime, while the transitional regime envelops both the laminar and turbulent frequency ranges. For the pulsatile flow at both Womersley numbers, the total TKE-frequency line matches the Kolmogorov spectrum for frequencies in the range of 35–100 Hz for the laminar regime and 35–80 Hz for the transitional regime. In the turbulent regime, frequency ranges of 35–85 Hz for the $\alpha = 4$ case and 20–95Hz for the $\alpha = 12$ case are observed. Hence, for the $\alpha = 4$ case, where the flow is noted to be highly influenced by the pulsatile cycle, the lower frequency bound did not change across the regimes.

For the steady flow case and the $\alpha = 12$ case—which was reported to mimic steady flow—a drop of the lower frequency bound is observed at the critical Reynolds number (from about 35Hz to 10Hz in the steady case; from about 35Hz to 18Hz in the $\alpha = 12$ case). This suggests that for low Womersley numbers, the unsteady term in the pulsatile flow influences the low-Hz instantaneous frequencies to a greater extent than turbulent flow structures. Conversely, for steady and high Womersley number flows, the presence of turbulent flow structures drives the lower frequency bound and any pulsatility-induced unsteadiness is secondary. The dynamics of the upper frequency bound were different for each case. Specifically, for the $\alpha = 12$ case, the upper frequency bound decreased in transition and then recovered to its laminar value in turbulence. This finding implies that the pulsatility-induced unsteady flow behaviors for high Womersley number flows influence the high-frequency flow dynamics. Only in the transitional flow regime, are the turbulent flow behaviors strong enough to influence this effect. For the $\alpha = 4$ case, the upper frequency bound similarly decreases in transition, and then does not significantly change in the turbulent regime. Hence, this indicates a scaling-type effect, where the flow scales derived from the unsteadiness are primarily low-frequency (about 35Hz), while for high Womersley flows they are high-frequency (about 90Hz). Moreover, because transitional and turbulent flow structures maintain frequencies in the range of about 10–30Hz, this finding may provide an explanation for why low Womersley number flows have been noted to maintain differing transitional flow dynamics as compared to steady flow while high Womersley number flows are steady-mimicking. For the steady case, the upper frequency bound increased to its highest value in transition, then decreased to below the laminar value in the turbulent regime. Hence, for steady flow, the largest frequency range was observed in transition, while for both unsteady cases, the smallest frequency range was observed in transition. This suggests that, to some extent, the unsteady flow behaviors potentially maintain a destructive interference with the developing transitional puffs and slugs. This finding and the

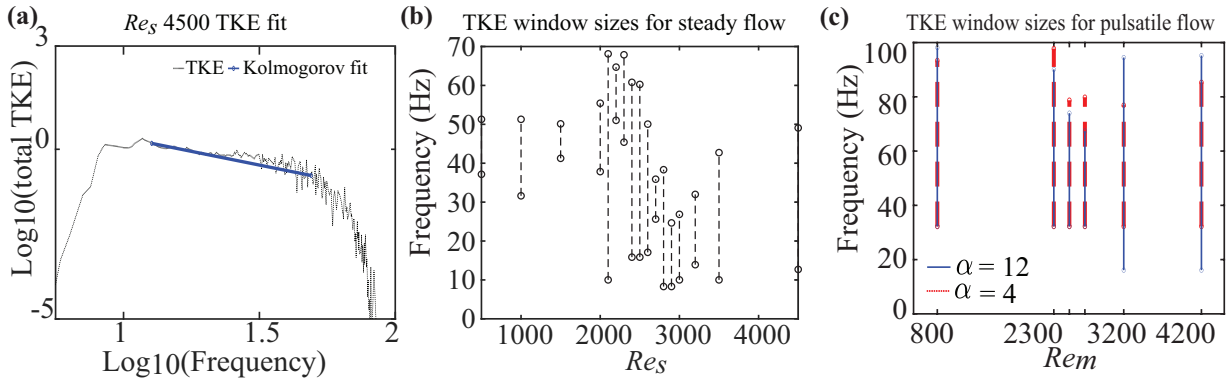

FIG. 12. (a) Demonstration of the Kolmogorov spectrum fit to the total TKE vs. frequency array for steady flow, $Re_s = 4500$ case. Minimum and maximum frequency ranges for which the total TKE arrays match the Kolmogorov spectrum for the (b) steady flow dataset and (c) pulsatile flow datasets.

possible interaction of the two distinct flow structure types should be explored further in future work.

V. CONCLUSION

In this work, we explore the efficacy of using the instantaneous frequency of the fluctuating velocity field to characterize the onset and development of transitional flow in pipes. Two experimental datasets including both steady-mean and pulsatile (unsteady-mean) pipe flow were used. Instantaneous dominant frequency of the fluctuating velocities of these datasets were evaluated using a novel Wavelet Hilbert Time Frequency (WHTF) analysis method presented herein. We demonstrated the accuracy of our WHTF method using analytical signals and highlighted its suitability for evaluating the TF representation of transitional and turbulent flows. The frequency analysis of the two flow datasets demonstrated clear differences in the instantaneous frequency structures across the laminar, transitional, and turbulent flow regimes. Specifically, we found that turbulent puffs and slugs generated during the transitional flow regime are low-frequency structures. Thus, this causes the centerline frequency of the pipe to drop significantly in the transitional regime. Additionally, the area of the frequency structures were observed to increase as the flow became transitional and turbulent. The transitional regime maintained the highest coherence of frequency structures, while the laminar regime maintained the lowest. Finally, we observed that the frequency range for which the total TKE spectrum matches the Kolmogorov spectrum is lower in frequency magnitude for turbulent flow as compared to laminar flow. Hence, these results revealed various characteristics of transitional and turbulent flow development as well as metrics that quantify this progression. Future work should aim to more specifically assess the behavior of these TF-metrics within specific stages of transition (e.g., sub-critical transition from 2D to 3D state, super-critical transition from 3D transition to 3D turbulence). Overall, this work takes a first step towards developing a universal metric capable of estimating transitional flow development for a pipe flow environment. Future work should focus on non-dimensionalizing the characteristic metrics identified herein to improve their universality.

VI. ACKNOWLEDGEMENTS

The authors gratefully acknowledge the funding for this project from the American Heart Association (AHA) grant # 940354 as well as the National Science Foundation grant # 2335760.

VII. AUTHOR DECLARATIONS

The authors state no conflict of interest.

VIII. DATA AVAILABILITY

The data that supports the findings of this study are available from the corresponding author upon reasonable request.

[1] M. Avila, D. Barkley, and B. Hof, Transition to turbulence in pipe flow, Annual Review of Fluid Mechanics **55**, 575 (2023).
[2] D. Barkley, Simplifying the complexity of pipe flow, Physical Review E **84**, 016309 (2011).
[3] T. M. Schneider, B. Eckhardt, and J. Vollmer, Statistical analysis of coherent structures in transitional pipe flow, Physical Review E **75**, 066313 (2007).
[4] T. M. Schneider and B. Eckhardt, Lifetime statistics in transitional pipe flow, Physical Review E **78**, 046310 (2008).
[5] R. T. Cerbus, Prandtl-tietjens intermittency in transitional pipe flows, Physical Review Fluids **7**, L011901 (2022).
[6] K. Haddad, Ö. Ertunç, M. Mishra, and A. Delgado, Pulsating laminar fully developed channel and pipe flows, Physical Review E **81**, 016303 (2010).
[7] J. Rolland, Extremely rare collapse and build-up of turbulence in stochastic models of transitional wall flows, Physical Review E **97**, 023109 (2018).
[8] G. K. Batchelor, *An introduction to fluid dynamics* (Cambridge university press, 1967).
[9] W.-J. Wang, S. Li, W. Huang, Z. Han, and W.-H. Wang, A unified friction factor formulation: Bridging laminar and turbulent friction factor with critical points analysis, Physics of Fluids **36** (2024).
[10] D. Morón and M. Avila, Turbulent puffs in transitional pulsatile pipe flow at moderate pulsation amplitudes, Physical Review Fluids **9**, 024601 (2024).
[11] M. R. Roach, S. Scott, and G. G. Ferguson, The hemodynamic importance of the geometry of bifurcations in the circle of willis (glass model studies), Stroke **3**, 255 (1972).
[12] K. M. Saqr, S. Tupin, S. Rashad, T. Endo, K. Niizuma, T. Tominaga, and M. Ohta, Physiologic blood flow is turbulent, Scientific reports **10**, 15492 (2020).

[13] D. Han, Y. Guo, P. Jiao, Y. Yuan, Y.-T. Lin, and Z. He, Coherent structures, turbulence intermittency, and anisotropy of gravity currents propagating on a rough and porous bed, Physics of Fluids **35** (2023).

[14] S. Mukherjee, R. K. Singh, M. James, and S. S. Ray, Intermittency, fluctuations and maximal chaos in an emergent universal state of active turbulence, Nature Physics , 1 (2023).

[15] R. Trip, D. Kuik, J. Westerweel, and C. Poelma, An experimental study of transitional pulsatile pipe flow, Physics of Fluids **24** (2012).

[16] A. Cicone, W. S. Li, and H. Zhou, New theoretical insights in the decomposition and time-frequency representation of nonstationary signals: the imfogram algorithm, Applied and Computational Harmonic Analysis **71**, 101634 (2024).

[17] M. R. Mangan, H. J. Oldroyd, K. T. Paw U, J. Clay, S. A. Drake, J. Kelley, and K. Suvočarev, Integrated quadrant analysis: A new method for analyzing turbulent coherent structures, Boundary-Layer Meteorology **184**, 45 (2022).

[18] S. Morales and M. E. Bowers, Time-frequency analysis methods and their application in developmental eeg data, Developmental cognitive neuroscience **54**, 101067 (2022).

[19] M. Pal, P. Manimaran, and P. K. Panigrahi, A multi scale time–frequency analysis on electroencephalogram signals, Physica A: Statistical Mechanics and its Applications **586**, 126516 (2022).

[20] J. R. Torres-Castillo, C. O. Lopez-Lopez, and M. A. Padilla-Castaneda, Neuromuscular disorders detection through time-frequency analysis and classification of multi-muscular emg signals using hilbert-huang transform, Biomedical Signal Processing and Control **71**, 103037 (2022).

[21] N. Shirdade, J. Joy Kolliyil, B. A.-d. El-khader, and M. Brindise, Developing a universal metric to assess the progression of transition to turbulence in pulsatile pipe flow, Bulletin of the American Physical Society (2023).

[22] J. Joy Kolliyil, N. Shirdade, and M. C. Brindise, Investigating intermittent behaviors in transitional flows using a novel time-frequency-based method, Experiments in fluids **65** (2024).

[23] J. Joy Kolliyil, N. Shirdade, and M. Brindise, A multi-wavelet frequency sift analysis method for analyzing intermittency in transitional flow, Bulletin of the American Physical Society **67** (2022).

[24] N. E. Huang, Z. Shen, and S. R. Long, A new view of nonlinear water waves: the hilbert spectrum, Annual review of fluid mechanics **31**, 417 (1999).

[25] N. E. Huang, M.-L. C. Wu, S. R. Long, S. S. Shen, W. Qu, P. Gloersen, and K. L. Fan, A confidence limit for the empirical mode decomposition and hilbert spectral analysis, Proceedings of the Royal Society of London. Series A: Mathematical, Physical and Engineering Sciences **459**, 2317 (2003).

[26] K. V. Bulusu and M. W. Plesniak, Shannon entropy-based wavelet transform method for autonomous coherent structure identification in fluid flow field data, Entropy **17**, 6617 (2015).

[27] Y. Zhou, *Hydrodynamic Instabilities and Turbulence: Rayleigh–Taylor, Richtmyer–Meshkov, and Kelvin–Helmholtz Mixing* (Cambridge University Press, 2024).

[28] Y. Zhou, Rayleigh–taylor and richtmyer–meshkov instability induced flow, turbulence, and mixing. I, Physics Reports **720-722**, 1 (2017), Rayleigh-Taylor and Richtmyer-Meshkov instability induced flow, turbulence, and mixing. I.

[29] Y. Zhou, Unification and extension of the similarity scaling criteria and mixing transition for studying astrophysics using high energy density laboratory experiments or numerical simulations, Physics of Plasmas **14** (2007).

[30] B. A.-D. T. El-Khader and M. C. Brindise, Effect of the womersley number on transition to turbulence in pipe flow: An experimental study, Physics of Fluids **36** (2024).

[31] R. Camussi and S. Meloni, On the application of wavelet transform in jet aeroacoustics, Fluids **6**, 299 (2021).

[32] T. Elperin and M. Klochko, Flow regime identification in a two-phase flow using wavelet transform, Experiments in fluids **32**, 674 (2002).

[33] M. Farge, Wavelet transforms and their applications to turbulence, Annual review of fluid mechanics **24**, 395 (1992).

[34] W.-Z. Yue, G. Tao, and Z.-W. Liu, Identifying reservoir fluids by wavelet transform of well logs, SPE Reservoir Evaluation & Engineering **9**, 574 (2006).

[35] L. Zou, L. Jing, and V. Cvetkovic, Roughness decomposition and nonlinear fluid flow in a single rock fracture, International Journal of Rock Mechanics and Mining Sciences **75**, 102 (2015).

[36] H. H. Bafroui and A. Ohadi, Application of wavelet energy and shannon entropy for feature extraction in gearbox fault detection under varying speed conditions, Neurocomputing **133**, 437 (2014).

[37] H. Zheng, Z. Li, and X. Chen, Gear fault diagnosis based on continuous wavelet transform, Mechanical systems and signal processing **16**, 447 (2002).

[38] H. Wang, C. Zhang, and X. Nie, Research on extraction and application of weak signals based on wavelet transform, Journal of Computers **28**, 288 (2017).

[39] N. Deng and C.-s. Jiang, Selection of optimal wavelet basis for signal denoising, in *2012 9th International Conference on Fuzzy Systems and Knowledge Discovery* (IEEE, 2012) pp. 1939–1943.

[40] S. Haque and T. Takara, Optimal wavelet for bangla vowel synthesis, International Journal of Scientific and Engineering Research **2** (2011).

[41] F. Scarano, Iterative image deformation methods in PIV, Measurement science and technology **13**, R1 (2001).

[42] A. C. Eckstein, J. Charonko, and P. Vlachos, Phase correlation processing for DPIV measurements, Experiments in Fluids **45**, 485 (2008).

[43] A. Eckstein and P. P. Vlachos, Digital particle image velocimetry (DPIV) robust phase correlation, Measurement Science and Technology **20**, 055401 (2009).

[44] J. Westerweel and F. Scarano, Universal outlier detection for piv data, Experiments in fluids **39**, 1096 (2005).

[45] M. C. Brindise and P. P. Vlachos, Proper orthogonal decomposition truncation method for data denoising and order reduction, Experiments in Fluids **58**, 1 (2017).

[46] S. He and J. Jackson, An experimental study of pulsating turbulent flow in a pipe, European Journal of Mechanics-B/Fluids **28**, 309 (2009).
[47] J. Stettler and A. F. Hussain, On transition of the pulsatile pipe flow, Journal of fluid mechanics **170**, 169 (1986).
[48] M. C. Brindise and P. P. Vlachos, Pulsatile pipe flow transition: Flow waveform effects, Physics of Fluids **30** (2018).
[49] M. Ö. Çarpinlioğlu, An overview on pulsatile flow dynamics, Journal of Thermal Engineering **1**, 496 (2015).
[50] G. K. Batchelor, On steady laminar flow with closed streamlines at large reynolds number, Journal of Fluid Mechanics **1**, 177 (1956).